crystals

MDPI

Article

$Ba_{0.9}A_{0.1}MnO_3$ (A = Ce, La, Mg) Perovskite-Type Mixed Oxides: Effect of Partial Substitution of Ba on the Catalytic Performance for the Oxidation of CO in Simulated Automobile Exhaust Conditions

Nawel Ghezali, Álvaro Díaz Verde and María José Illán Gómez *

MCMA Group, Inorganic Chemistry Department, Institute of Materials of the University of Alicante (IUMA), Faculty of Sciences, University of Alicante, 03690 Alicante, Spain; gn11@alu.ua.es (N.G.); alvaro.diaz@ua.es (Á.D.V.)

* Correspondence: illan@ua.es

Abstract: $BaMnO_3$ (BM) and $Ba_{0.9}A_{0.1}MnO_3$ (BM-A) (A = Ce, La or Mg) perovskite-type mixed oxides were synthesized by the aqueous sol–gel method; thoroughly characterized by ICP-OES, XRD, H_2-TPR, BET, and O_2-TPD; and tested as catalysts for CO oxidation under simulated automobile exhaust conditions. The characterization results indicate that the main effects of the partial substitution of Ba with A-metal in BM perovskite are the maintenance of the hexagonal structure of the perovskite and the increase in reducibility and oxygen mobility. All samples catalyze the CO to CO_2 oxidation reaction in the different reactant mixtures employed, showing the best performance for the mixture with the lowest CO/O_2 ratio and in the presence of a dopant in the BM perovskite formulation. BM-La is the most active catalyst for improving CO oxidation, as it is the most reducible, and because is able to evolve oxygen at intermediate temperatures.

Keywords: perovskite-type mixed oxides; sol–gel synthesis; CO oxidation; simulated automobile exhaust; Ce; La; Mg; Mn

Citation: Ghezali, N.; Díaz Verde, Á; Illán Gómez, M.J. $Ba_{0.9}A_{0.1}MnO_3$ (A = Ce, La, Mg) Perovskite-Type Mixed Oxides: Effect of Partial Substitution of Ba on the Catalytic Performance for the Oxidation of CO in Simulated Automobile Exhaust Conditions. *Crystals* **2024**, *14*, 191. https://doi.org/10.3390/cryst14020191

Academic Editor: Bo Chen

Received: 13 December 2023
Revised: 10 January 2024
Accepted: 12 February 2024
Published: 14 February 2024

1. Introduction

The reduction in the harmful emissions of CO from several sources, particularly from automobile exhaust [1–3], is mandatory to adhere to the European Climate Legislation [4], according to which the European Union (EU) will be climate neutral by 2050. Usually, noble metal-based catalysts are employed for CO oxidation as they present higher catalytic activity than transition metals [5]. Specifically, Pt, Pd, Ag, Ru, Ir, and Rh noble metals have been used as active components of the Three-Way Catalysts (TWCs) [6–10]. As using noble metal-based catalysts for CO oxidation is limited by its prohibitive cost [11,12], the challenge is the design of efficient (i.e., with high activity and with long-term stability) noble-metal free catalysts (or with very low content) that adhere to the present and future legislation for automotive emissions [13]. Thus, developing a new generation of catalysts for CO oxidation in automobile exhaust conditions is imperative [14]. So, to achieve this purpose, the first step is to reduce the amount of noble metals in the catalytic formulations by using supported catalysts, in which the role of support (in the case of catalytically active supports) is not only the stabilization of the metallic particles by minimizing or avoiding their sintering [15], but also providing additional active sites for the reaction. In fact, current TWCs are based on noble metals supported on ceria, presenting highlighted catalytic properties due to their high Oxygen Storage Capacity (OSC), which allows a rapid release of oxygen based on the redox properties of the Ce(IV)/Ce(III) pair [16,17]. Thus, the next step would consist in the design of noble metal-free catalysts with a catalytic performance close to those shown by noble metal formulations.

In line with this, in recent decades, perovskite-type mixed oxides (general composition ABO_3) have been used as catalysts for different processes [18–24] and have also been promising catalysts for removal of the pollutants emitted by Gasoline Direct Injection (GDI) engines [18,19]. Their popularity arises from the easy fitting of their physical and chemical properties, which enables the creation of specific and tailored active sites for the selected reaction [25,26]. This flexibility is crucial to optimize the catalytic performance for a wide spectrum of reactions [22]. The incorporation of metals with different oxidation states by the partial substitution of A and/or B cations leads to structural defects, such as anionic or cationic vacancies, or modifications in the oxidation state of the B metal (usually a transition metal) [12,18,24,27], that could significantly enhance the catalytic activity [28]. According to previous results [14,22,29], manganese-based perovskites are promising catalysts for CO oxidation reactions, as this metal presents atomic orbitals with the appropriate symmetry and energy levels for CO and O_2 activation. Thus, for Mn(III), the electronic configuration presents three electrons in the t_{2g} orbitals and one in the e_g orbitals, which allows effective interaction with CO molecules. So, the partially empty e_g orbital accepts the CO lone electron pair, and the back-donation of a t_{2g} electron to the antibonding π^* orbital of the CO molecule occurs as a pivotal step in CO activation. On the other hand, Mn(IV) presents three electrons in the t_{2g} orbitals, and the interaction with CO and O_2 is intricately tied to the strength of the Mn-O bond and, as the Mn-O bond strength diminishes, the catalytic activity for CO oxidation notably increases [30,31].

In a previous study [32], a series of $Ba_{0.9}A_{0.1}MnO_3$ (A = Ca, Ce, La, Mg, Sr) perovskite-type mixed oxides was synthesized, characterized, and tested for soot oxidation under simulated GDI exhaust conditions, and the results revealed that the samples presented a higher selectivity to CO_2 than a $BaMnO_3$ raw sample; thus, it seems that they could be effective as catalysts for CO oxidation. Consequently, this paper analyzes the catalytic activity of $Ba_{0.9}A_{0.1}MnO_3$ (A = Ce, La, Mg) perovskite-type mixed oxides, prepared by the sol–gel method, for CO oxidation in different conditions simulating different compositions of the automobile exhaust. The objective is to determine the effect of the partial substitution of Ba cation (by Ce, La, or Mg) on the catalytic performance for CO oxidation.

2. Materials and Methods

2.1. Synthesis of Catalysts

$Ba_{0.9}A_{0.1}MnO_3$ series (A = Ce, La, Mg, denoted as BM-A) was prepared by the sol–gel method adapted for being used in an aqueous medium [33]. The metal precursors employed are as follows: barium acetate ($Ba(CH_3COO)_2$, 99.0% purity, Sigma-Aldrich, St. Louis, MO, USA), lanthanum(III) nitrate hydrate ($La(NO_3)_3{*}H_2O$, 99.0% purity, Sigma-Aldrich), magnesium nitrate hexahydrate ($Mg(NO_3)_2{\cdot}6H_2O$, 99.0% purity, Sigma-Aldrich), cerium(III) nitrate hexahydrate ($Ce(NO_3)_3{\cdot}6H_2O$, 99.0% purity, Sigma-Aldrich), and manganese(II) nitrate tetrahydrate ($Mn(NO_3)_2{\cdot}4H_2O$, 99.0% purity, Sigma-Aldrich). To prepare the $BaMnO_3$ sample, ethylenediaminetetraacetic acid (EDTA, 98.5% purity, Sigma-Aldrich) and citric acid ($C_6H_8O_7$, 98.5% purity, Sigma-Aldrich) were employed as chelating agents (with 2 EDTA/Ba and citric acid/Ba molar ratios) to prevent the precipitation of metal precursors. To prepare the samples, a 40 mL solution of citric acid and the appropriate amount of metal precursors was heated until 60 °C and, after that, the gel was obtained by thermally stirring this solution at 65 °C for five hours. In the case of the $BaMnO_3$ reference sample, EDTA was incorporated into the solution before the metal precursors, and, finally, citric acid was included. A 30 wt% ammonia solution (from Panreac, Castellar del Vallès, Spain) was used to keep the pH at 8.5 throughout all the steps of the procedure. Subsequently, the gel was dried at 90 °C for 48 h and, finally, the powder was then calcined at 850 °C for 6 h.

2.2. Characterization

The techniques used for the characterization of samples were as follows:

I. Inductively Coupled Plasma Optical Emission Spectroscopy (ICP-OES), to determine the elemental composition. To obtain the solution needed for the analysis, a mixture of 5 mL of aqua regia and 10 mL of distilled water was used to dissolve 10 mg of catalyst. The analysis was performed in a PerkinElmer device, the Optimal 4300 DV (Waltham, MA, USA).
II. N_2 adsorption at −196 °C, carried out in an Autosorb-6B device from Quanta chrome (Anton Paar Austria GmbH, Graz, Austria), to obtain the specific surface area. Before the N_2 adsorption tests, the solids were degassed at 250 °C for 4 h.
III. X-Ray Diffraction (XRD) to identify the crystalline structure. The X-ray patterns were recorded with a Bruker D8-Advance device (Billerica, MA, USA), employing Cu K_α radiation at a step rate of 0.4°/min between 20° and 80° 2θ angles.
IV. Temperature-Programmed Reduction with H_2 (H_2-TPR), to test the reducibility. These tests were developed in a Pulse Chemisorb 2705 (from Micromeritics, Norcross, GA, USA) provided with a Thermal Conductivity Detector (TCD) for determining the change in the thermal conductivity of the gaseous mixture, which is exclusively due to the decrease in the H_2 amount (by its consumption during the reduction of samples), as the effect due to the water vapor (generated as oxidation product) has been avoided by its condensation before the entrance to the TCD. To develop the tests, 30 mg of a sample was heated at 10 °C/min from 25 °C to 1000 °C in a 5% H_2/Ar environment (40 mL/min). Copper (II) oxide (CuO, 99.9% purity, Sigma-Aldrich) was employed as reference to quantify the amount of H_2 consumed.
V. Temperature-Programmed Desorption of O_2 (O_2-TPD) experiments, to estimate the O_2 evolved from the samples. These studies were conducted using a Thermal Gravimetric Mass Spectrometry system (TG-MS, Q-600-TA, and Thermostar from Balzers Instruments (Pfeiffer Vacuum GmbH, Germany and Balzers, Liechtenstein), and 16 mg of sample heated at 10 °C/min from room temperature to 950 °C in a 100 mL/min He gas flow. All samples underwent a 1 h preheating process at 150 °C to remove moisture before testing. For the quantification of evolved H_2O, CO, O_2, and CO_2, the 18, 28, 32, and 44 m/z signals were analyzed. A CuO reference sample (CuO, 99.9% purity, Sigma-Aldrich) was employed to calculate the amount of generated oxygen.

2.3. Activity Tests

For the CO oxidation tests, three reactant mixtures were employed: (i) 1% CO + 1% O_2 in He, as an approximation to the CO concentration in the actual Three-Way Catalyst (TWC) working conditions, (ii) 1% CO + 10% O_2 in He, for analyzing the effect of using a higher oxygen concentration compared to (i), and (iii) 0.1% CO + 10% O_2 in He, for simulating the oxidation of a very low CO percentage, which simulates the conditions found in a Diesel Oxidation Catalytic Converter (DOC), or the exhaust of oxy-fuel combustion engines (excess of O_2 and very low amount of CO) [34]. The CO oxidation experiments were performed in a U-shaped quartz reactor filled with a mixture of 50 mg of catalyst and 100 mg of SiC (used for avoiding the overpressure inside the reactor). Two types of experiments were developed using a gas flow of 100 mL/min: (i) Temperature-Programmed Reaction conditions (CO-TPR) from room temperature to 500 °C and using a 10 °C/min heating rate, and ii) isothermal reactions at 300 °C during 3 h, using the 1% CO + 1% O_2 reactant mixture. To clean the surface of samples, the catalyst-SiC mixture was pre-heated for 1 h at 500 °C in a 5% O_2/He gas mixture. An Agilent 8860 Gas Chromatograph (Agilent Technologies Spain, Madrid, Spain), equipped with a Thermal Conductivity Detector and two packed columns (Porapack-Q and MolSieve-13X (Agilent Technologies Spain, Madrid, Spain)), was used for the reaction products quantification.

The CO conversion was determined using Equation (1):

$$\text{CO conversion } (\%) = \frac{(CO_{in} - CO_{out})}{CO_{in}} \cdot 100 \quad (1)$$

where CO_{in} is the inlet molar flow rate of CO, and CO_{out} is the outlet molar flow rate of CO which has not been oxidized to CO_2.

3. Results and Discussion

3.1. Characterization

Nomenclature and the most relevant characterization information, including the A (Ce, La or Mg) metal content (obtained by ICP-OES), the BET surface area (calculated from N_2 adsorption data), and some XRD data of the tested samples, are listed in Table 1. The Williamson-Hall method [35] was used to estimate the average crystallite size, and the cell parameters of the hexagonal perovskite phase ($a = b \neq c$) were determined by using the main XRD peak. The doping of $BaMnO_3$ with Ce, La, or Mg leads to an increase in the specific surface area but, as expected for perovskite-type mixed oxides, very low values were obtained for all samples due to the almost undeveloped porosity. According to K. Akinlolu et al. [36], the very low porosity development is a consequence of the calcination temperature (850 °C) used in the synthesis. The ICP-OES data showed that the sol–gel process allowed the addition of the required percentage of dopants (Ce, La, or Mg).

Table 1. Nomenclature and characterization data.

Nomenclature	Molecular Formula	BET Surface Area (m^2/g)	A (wt%)	Intensity (a.u) [a]	Average Crystal Size (nm)	Cell Parameters (Å) [b]	
						a	c
BM	$BaMnO_3$	3	-	1154	46	5.7	4.9
BM-Ce	$Ba_{0.9}Ce_{0.1}MnO_3$	10	1.3	1913	22	5.5	5.0
BM-La	$Ba_{0.9}La_{0.1}MnO_3$	7	1.1	1562	28	5.7	4.8
BM-Mg	$Ba_{0.9}Mg_{0.1}MnO_3$	7	4.2	2382	28	5.7	4.8

[a] Corresponding to the main XRD hexagonal perovskite peak, [b] Calculated using the main XRD hexagonal perovskite peak.

The XRD patterns of the BM and BM-A samples are featured in Figure 1. All samples present the hexagonal ABO_3 perovskite structure as the main crystal phase, since the detected signals correspond to the XRD pattern of $BaMnO_3$ perovskite (hexagonal 2H-$BaMnO_3$, PDF number: 026-0168, designated by the International Centre of Diffraction Data, (ICDD)) [37]. In addition, based on the literature [38], this structure is composed of chains of face-sharing MnO_6 units rather than corner-sharing MnO_6 units. The substitution of Ba cation with Ce, La, or Mg cations does not significantly modify the diffraction pattern observed for the raw perovskite, because the position of the main diffraction peak of the pervoskite is not appreciably modified (see Figure 1b), and only $Ba_3Mn_2O_8$, MnO_2 and CeO_2 (PDF numbers: 073-0997 024-0735, and 043-1002043-1002, respectively) have been identified as segregated minority phases. However, the data in Table 1 reveal (i) an increase in the intensity of the main diffraction peak of hexagonal perovskite which is more pronounced for BM-Mg, probably due to the higher content in Mg respect to Ce or La; (ii) an increase in the crystallinity, which seems being related to the decrease in the average crystal size for BM-A samples; and, finally, (iii) a slight deformation of the structure, as *a* and *c* cell parameters slightly decrease, being this modification more significant also for BM-Ce perovskite. The decrease in the cell parameters is a consequence of the different ionic radii of Ba(II) and A cations (included in Table 2). Note that Ce(IV) and Ce(III) present the lowest ionic radii among the A cations located in Ba(II) sites in the perovskite lattice (so Ce and La). Mg(II) presents an ionic radius even lower than Ce(III)/Ce(IV), but it was previously concluded [39] that this cation is located in the B position of the perovskite lattice since its radius is more similar to that of Mn(III) and Mn(IV) than to the Ba(II) cation. So, it seems that the partial substitution of Mn (by Mg(II)) in the B position of the perovskite lattice affects more to the intensity of the main diffraction peak of the hexagonal perovskite structure than the partial substitution of Ba (by Ce(III)/Ce(IV) or La(III)) in the A position.

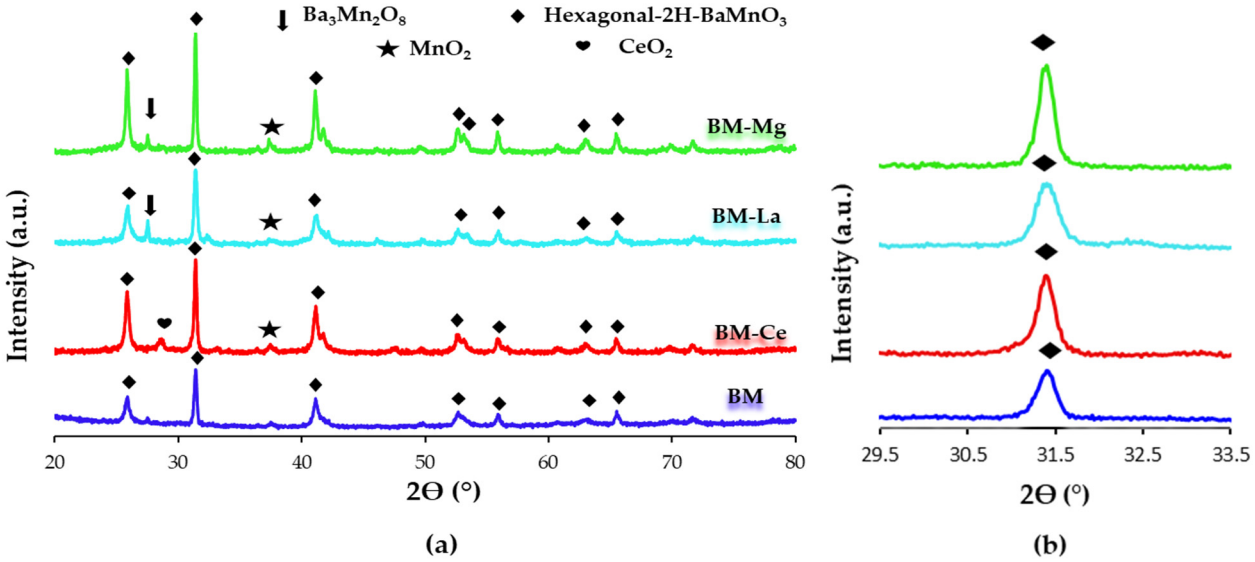

Figure 1. (**a**) XRD patterns and (**b**) magnification of the 2θ diffraction angle corresponding to the main diffraction peak of the hexagonal 2H-$BaMnO_3$ phase.

Table 2. Ionic radii of cations according to Goldschmidt correction [31,36,37,40].

Metals	Ba(II)	Mg(II)	La(III)	Ce(IV)	Ce(III)	Mn(IV)	Mn(III)
Ionic radii (pm)	146.4	65.0	107.3	90.6	105.2	53.0	65.0

The H_2-TPR experiments inform about [41,42]: (i) the redox properties, (ii) the mobility of oxygen through the surface and the bulk, and (iii) the stability of samples in a reducing atmosphere. During the H_2-TPR tests, H_2 is able to reduce high-valence metallic ions (usually those located in the B site of perovskite-type mixed oxides [43,44]) to low-valence metallic ions or metallic atoms, and surface and lattice oxygen ions can also participate in this reduction reaction [45]. The H_2-TPR profile for MnO_2 (presented in Figure 2a, used as reference and prepared using the same manganese precursor and identical calcination conditions than BM and BM-A perovskites) shows two overlapping peaks at around 400 and 500 °C, which, according to literature data [46], correspond to the reduction of manganese in two steps; firstly MnO_2/Mn_2O_3 to Mn_3O_4 and, subsequently, Mn_3O_4 to MnO. Usually [32,38,47,48], a multiple-step reduction was observed for the manganese-based samples, showing (i) an intense peak centered between 400–600 °C, corresponding to the Mn(IV) and Mn(III) reduction to Mn(II); (ii) a small peak from 700 °C to 800 °C due to the oxygen species reduction; and (iii) a third peak with a maximum between 900 °C and 1000 °C, corresponding to the Mn(III) to Mn(II) reduction in the bulk. In fact, in the H_2-TPR profiles of BM, BM-Ce, BM-La, and BM- Mg displayed in Figure 2a, these three H_2 consumption peaks are detected. The first sharp peak centered between 400 and 600 °C corresponds to both the Mn(IV) to Mn(III) reduction, and Mn(III) reduction to Mn (II) [38,49]. The second one, located at intermediate temperatures (between 700 °C and 800 °C), is a poorly defined peak attributed to the reduction in oxygen species and, finally, the peak detected at the highest temperatures (between 900 °C and 1000 °C) is assigned to the reduction of bulk Mn(III) to Mn(II). Note that the maximum of the peak corresponding to the reduction in the Mn(IV) species in the perovskite samples is shifted towards higher temperatures respect to the observed for MnO_2 reference sample [46,50]. This observation could be considered as evidence of the high interaction of Mn species with the other ions present in the perovskite lattice, that hinders the redox process. Moreover, regarding the BM-A samples, only the presence of La(III) and Mg(II) seems to modify the temperature corresponding to the maximum of the sharpest reduction peak, which is 499 °C for BM-

Mg and 468 °C for BM-La, versus 515 °C for BM, so, BM-La is the sample requiring the lowest temperature for reduction among the BM-A series. For BM-Mg, the decrease in the temperature could be due to an improved oxygen mobility due to the lower amount of Ba(II) in A sites (as Mg(II) is partially replacing Mn(IV)/Mn(III) in B site). For BM-La, the lower reduction temperature is the consequence of improved oxygen mobility due to the loss of oxygen from MnO_6 octahedra caused by the increase in the amount of Mn(III) that takes place to compensate the higher positive charge of La(III) respective to Ba(II). The area under the H_2 consumption profiles between 450 °C and 600 °C was used to determine the experimental hydrogen consumption per gram of the sample, and these values are compared in Figure 2b with the nominal hydrogen consumption calculated considering either Mn(IV) or Mn(III) as the unique manganese oxidation state. Regarding these results, Mn(IV) and Mn(III) oxidation states coexist in bulk for BM-Mg, BM-Ce, and BM-La, with Mn(IV) being the main oxidation state in the bulk of BM. These data seem to confirm that, for BM-Ce and BM-La, a higher amount of Mn(III) exists on the bulk of the perovskite in order to compensate the higher positive charge of Ce(IV) and La(III) with respect to Ba(II).

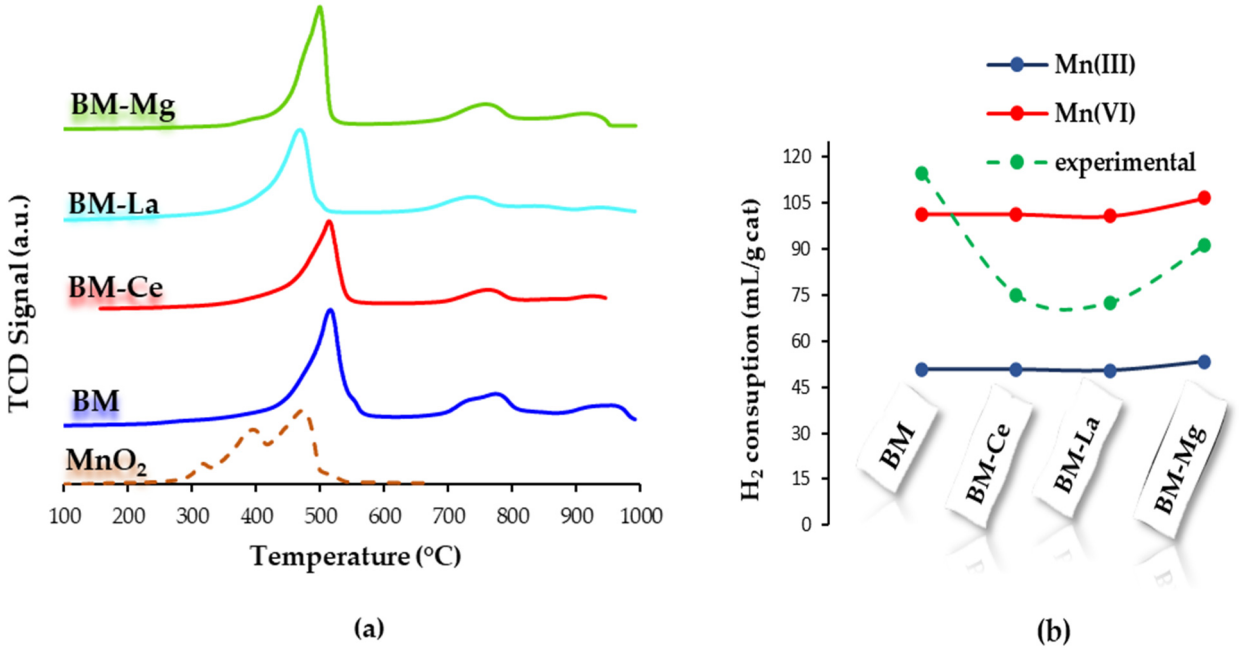

Figure 2. (**a**) H_2-TPR profiles and (**b**) H_2 consumption (mL/g of catalyst).

To determine the lability of the oxygen species present in the bulk of BM and BM-A samples, O_2-TPD experiments were developed. According to the literature [51], three desorption peaks are typically detected for perovskites during an O_2-TPD test: (i) the oxygen adsorbed on the surface (α-O_2) is released at temperatures below 350 °C; (ii) the desorption peak between 500 and 700 °C is attributed to the oxygen that comes from the adsorbed on the surface lattice defects (α'-O_2); and (iii) the peak observed at temperatures higher than 700 °C is related to the desorption of lattice oxygen (β-O_2). As shown in Figure 3, BM-Ce and BM-Mg samples mainly evolve oxygen from the perovskite lattice, which is promoted by the redox reactions involving the Mn(IV)/Mn(III) pair, and also, for BM-Ce, the Ce(IV)/Ce(III) pair. However, for BM-La, the oxygen desorbed mainly comes from that which is adsorbed on the surface lattice defects, while BM raw perovskite does not show a clear desorption peak. The total amount of O_2 (as μmol/g of sample), calculated from the area under the O_2 profiles (and using a CuO sample as a reference for quantification) is 114 for BM-Ce, 68 for BM-Mg, 61 for BM-La, and 23 for BM. So, these data indicate that the partial substitution of Ba cation (by Ce, La, or Mg) increases the amount of oxygen evolved by perovskite and, hence, the oxygen mobility is enhanced. Note that BM-Ce evolves the highest amount of oxygen (as β-O_2), due to the contribution of the

Ce(IV)/Ce(III) redox pair, and that BM-La generates oxygen at the lowest temperature as it comes from the adsorbed in the surface oxygen lattice vacancies (α'-O_2) [51]. As it was described above, for BM-La, the loss of oxygen from MnO_6 octahedra (so, the creation of lattice oxygen vacancies) is favored due to the presence of a higher amount of Mn(III) to compensate for the higher positive charge of La(III) versus Ba(II). Thus, BM-La seems to be the most unique BM-A sample, being able to release oxygen at T < 500 °C, which is in the range of interest for CO oxidation reaction.

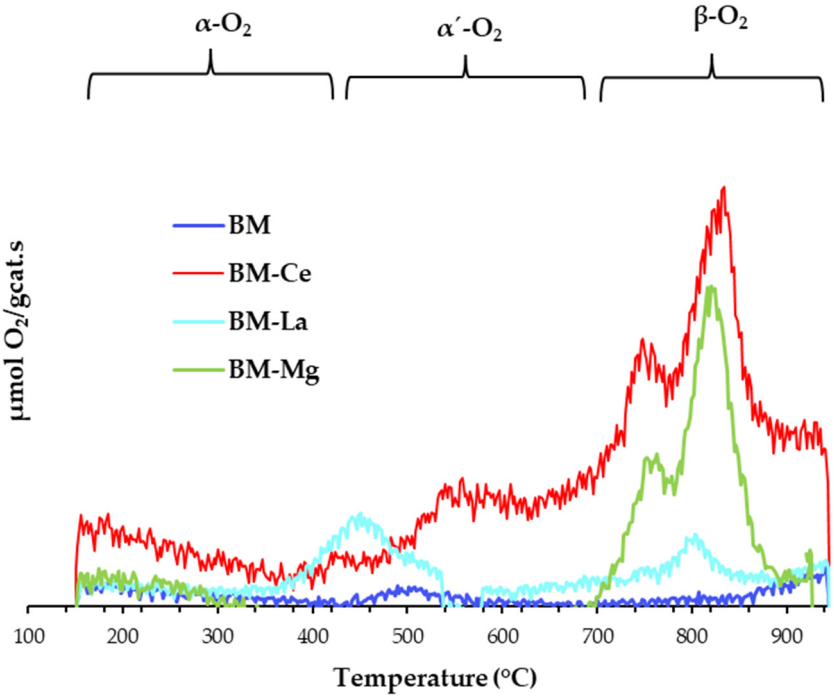

Figure 3. O_2-TPD profiles.

3.2. Catalytic Activity

The CO conversion profiles (CO-TPR) are shown in Figure 4, and the $T_{50\%}$ (°C) data (which is the temperature to achieve the 50% of CO conversion) are featured in Table 3. For comparative purposes, the profile corresponding to a commercial platinum-based catalyst (1% Pt/Al_2O_3, Pt-Al from Sigma Aldrich), used as a reference, has also been included. The CO conversion profiles and the $T_{50\%}$ data reveal that all the tested samples catalyze the CO oxidation reaction in the three reactant mixtures employed, as the gas phase reaction does not take place under 500 °C in the absence of a catalyst (uncatalyzed profile in Figure 4). These results could be expected, as it is well-known that Mn-based samples are effective catalysts for CO oxidation [52]. However, all samples present a lower capacity for increasing the percentage of CO conversion than the Pt-Al reference catalyst. Additionally, after the partial substitution of Ba cation, an increase in the CO conversion is observed for BM-A samples, as the CO-TPR profiles appear at lower temperatures and the $T_{50\%}$ values are lower than for the BM raw perovskite. So, the partial substitution of Ba cation seems to be an effective strategy to improve the catalytic performance for CO oxidation of BM perovskite. As could be expected (because it is the most reducible sample), BM-La seems to be the most active sample, presenting the closest performance to that of the Pt-Al reference.

However, the degree of improvement seems to depend on the sample and reaction atmosphere:

(i) In 1% CO + 1% O_2, BM-La is the best catalyst as it presents the highest lowering of $T_{50\%}$ (the most negative value of $\Delta T_{50\%}$) respect to BM (see Table 3).

(ii) In 1% CO + 10% O_2, in the presence of an excess of oxygen in the reaction atmosphere respect to (i), both BM-La and BM-Mg present a similar performance.
(iii) In 0.1% CO + 10% O_2, which was the lowest CO/O_2 ratio reactant mixture tested, the three samples feature a more similar performance.

Table 3. $T_{50\%}$ (°C) for CO oxidation.

Catalyst	1% CO + 1% O_2		1% CO + 10% O_2		0.1% CO + 10% O_2	
	$T_{50\%}$	$\Delta T_{50\%}$ *	$T_{50\%}$	$\Delta T_{50\%}$ **	$T_{50\%}$	$\Delta T_{50\%}$ ***
BM	400	---	455	55	340	−115
BM-Ce	325	−75	373	48	230	−143
BM-La	290	−110	320	30	250	−70
BM-Mg	342	−58	340	2	175	−165
Pt-Al	265	---	210	−55	130	−80

* Respect to $T_{50\%}$ of BM. ** Respect to $T_{50\%}$ in 1% CO + 1% O_2. *** Respect to $T_{50\%}$ in 1% CO + 10% O_2.

Thus, it seems that BM-La is the best catalyst tested in almost all the gas mixture compositions explored. Focusing the attention on the characterization data discussed in the previous section, it has to be underlined that BM-La is the sample presenting the highest reducibility (lower temperature for the maximum of the main reduction peak in H_2-TPR tests) and the only catalyst evolving oxygen at intermediate temperature (α'-O_2). Thus, it appears that these two properties are relevant for enhancing CO oxidation. In this sense, P. Doggali et al. [21] also concluded that the partial substitution of A site improves the catalytic activity of $LaCoO_3$ as the $La_{0.8}Ba_{0.1}CoO_3$ catalyst exhibits a superior catalytic performance for both CO and particulate matter oxidation.

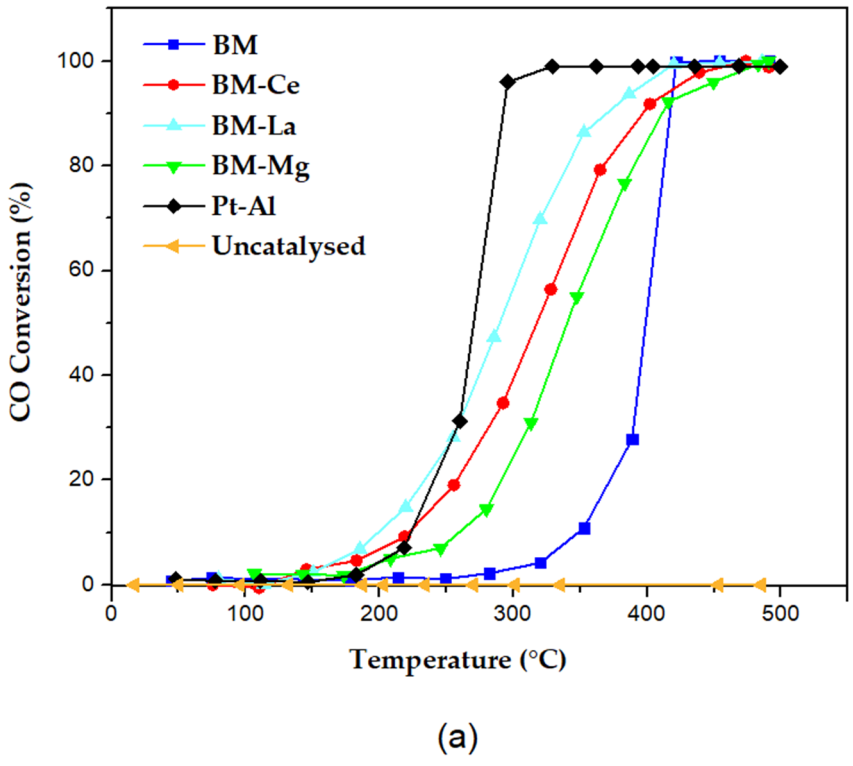

(a)

Figure 4. *Cont.*

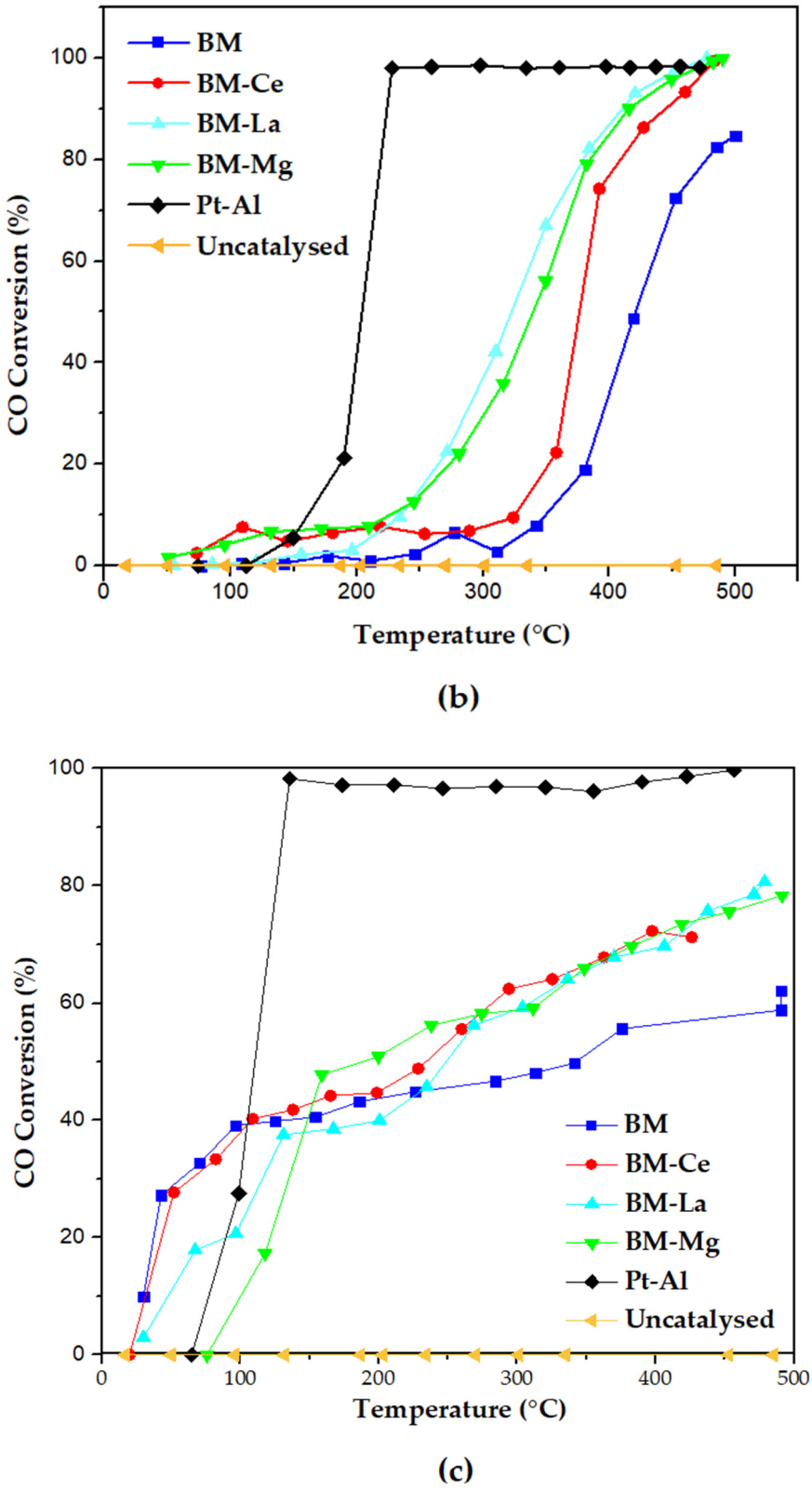

Figure 4. CO-TPR conversion profiles in (**a**) 1% CO + 1% O_2, (**b**) 1% CO + 10% O_2 and (**c**) 0.1% CO + 1% O_2.

The performance in the different reactant mixtures used has been compared in terms of the $T_{50\%}$ values collected in Table 3. Thus, it seems that if the oxygen percentage increases from 1% to 10%, $T_{50\%}$ is higher (so the samples are less active for catalysing the CO

oxidation) for BM, BM-Ce, and BM-La, but the opposite is observed for Pt-Al reference and, finally, it does not appreciably change for BM-Mg. The different response of BM-Mg sample versus an increase in the O_2 percentage (from 1% to 10%) is probably related to the different location of Mg in the lattice, which is in the B cation position of ABO_3 perovskite (that is, partially replacing Mn) instead of replacing Ba cation in the A site. Additionally, holding a 10% O_2, the further lowering in the CO percentage from 1% to 0.1% provokes a decrease in the $T_{50\%}$ for all samples, indicating an improvement of the performance for catalysing CO oxidation. On the other hand, note that the most intense decrease is detected for BM-Mg and BM-Ce, presenting BM-La the lowest change. Thus, BM-La is not only the most effective among BM-A samples in decreasing $T_{50\%}$ respect to the raw perovskite (BM), but it also presents the most stable performance versus fluctuations in O_2 and CO concentrations, being even more stable than the platinum-based catalyst. This fact would be interesting for practical applications. Finally, comparing $T_{50\%}$ data in the different reactant mixtures, it is concluded that all samples, as well as the Pt-Al reference, are more effective in catalyzing the CO oxidation in the 0.1% CO + 10% O_2, as they present the lowest values of $T_{50\%}$. In this sense, S. Zheng et al. [53] also concluded that $LaMn_{0.4}Fe_{0.6}O_3$ (synthesized using the rota-vapor citrate method) showed the highest CO oxidation activity in a 1% CO and 20% O_2, showing a $T_{50\%}$ of 375 °C which is similar to the featured by BM-Ce sample in 1% CO + 10% O_2 gas mixture.

To understand the catalytic performance shown by the tested samples, the mechanisms proposed in the literature for CO oxidation reactions have been revised. It is well known that these mechanisms are highly dependent not only on the reaction temperature, and on the CO and O_2 [54–56] percentages, but also on the type of catalysts and, for perovskite type mixed oxides, two mechanisms are generally accepted [57]:

- the Langmuir-Hinshelwood (LH) mechanism, which involves the adsorption of CO and O_2 molecules, followed by their reaction to form OOCO intermediates [13]. This step is considered the rate-limiting one of the oxidation processes.
- the Eley-Rideal (ER) mechanism, in which the activated (adsorbed) O_2 molecules combine directly with the CO molecules in the gas phase, being the activation of O_2 the rate-limiting step.

Among these two proposed mechanisms, the LH mechanism has been suggested for CO oxidation in the presence of oxygen vacancies, in which the preferential adsorption of oxygen will take place to generate highly reactive oxygen species (such as O^{1-}) [58,59].

Thus, to discuss the results obtained, it can be assumed that the LH mechanism is working for perovskites and that the CO molecules adsorbed on the catalyst surface will react with the adsorbed O_2 and, subsequently, the CO_2 generated will desorb. In this sense, Royer et al. [60] suggested that, if a strong CO inhibition is detected, it means that the two gases compete by the same adsorption sites. On the other hand, if a low CO reactant mixture is used (i.e., 1% CO + 10% O_2 or 0.1% CO + 10% O_2), oxygen will be preferentially chemisorbed on the surface oxygen vacancies as it is in excess and, subsequently, the CO molecules will be also adsorbed on the remaining free active sites [52,61].

Taking in mind all these considerations, it seems that in BM and BM-A samples, CO and O_2 compete by the same active sites where these two molecules will be adsorbed to react following the LH mechanism. As $T_{50\%}$ increases if O_2 concentration is increased from 1% to 10%, it means that O_2 is initially adsorbed and, subsequently, CO is also adsorbed in the free active sites. This sequence also explains that $T_{50\%}$ decreases when CO percentage is decreased from 1% to 0.1%, as a more effective activation of CO will take place because a lower number of active sites is needed.

Finally, two cycles of isothermal reaction at 300 °C in 1% CO + 1% O_2 gas mixture have been developed to deeper analyze the catalytic performance, being the CO conversion profiles shown in Figure 5. In general terms, the CO conversion percentages are similar to those obtained during CO-TPR (shown in Figure 4a): BM-La (65%) > BM-Ce (52%) > BM-Mg (35%) > BM (15%) and, almost stable profiles are shown for all samples. Thus, it seems that, as concluded by other authors [62], the perovskites do not suffer an appreciable

deactivation during 3 h of reaction time, so, a long lifetime is expected when they would be used as catalysts for CO oxidation.

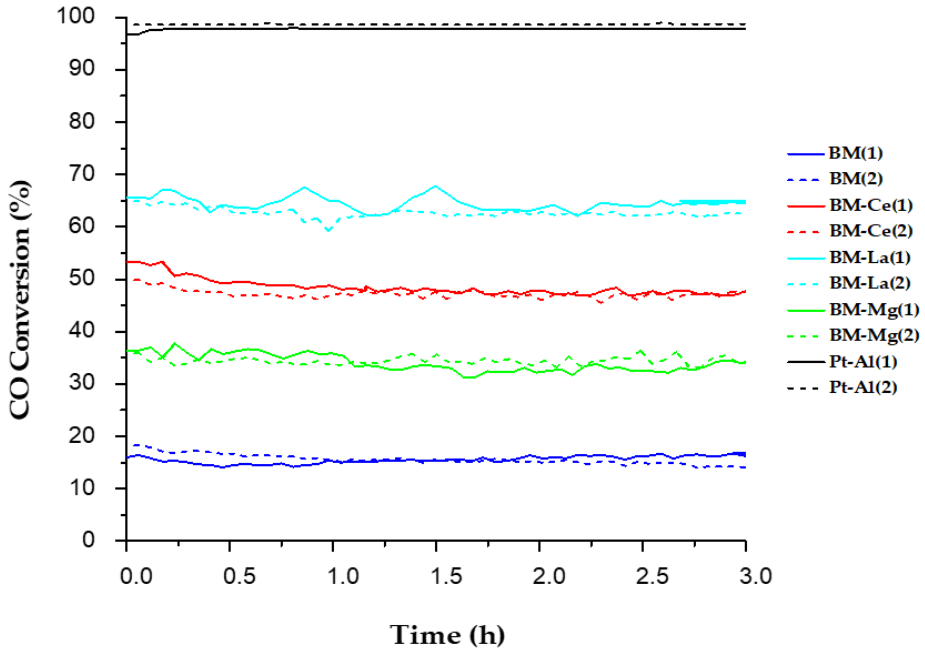

Figure 5. CO conversion profiles at 300 °C in 1% CO + 1% O_2.

Thus, in the presence of BM-A a higher percentage of CO conversion is achieved than if BM is used, it is confirmed that the partial substitution of Ba cation by Ce, La, or Mg allows the improvement of catalytic performance. It is also proven that BM-La is the most active catalyst for CO oxidation, as it is the most easily reducible and because is the only one evolving oxygen at intermediate temperatures, which seems to be effective for CO oxidation.

4. Conclusions

From the above discussed characterization and conversion data, the main conclusions obtained are as follows:

- Despite the partial substitution of Ba with Ce, La, or Mg, the mixed oxides maintain the hexagonal $BaMnO_3$ perovskite structure.
- The partial substitution of Ba by Ce, La, or Mg seems to enhance the mobility of oxygen and the reducibility of the samples, BM-La being the most reducible sample and the unique evolving oxygen at intermediate temperatures (α'-O_2).
- All perovskites-type mixed oxides catalyze CO oxidation under the different reactant mixtures tested, showing the lowest $T_{50\%}$ values for the lowest CO/O_2 ratio gas mixture used (0.1% CO + 10% O_2).
- The samples do not suffer an appreciable deactivation during reaction at 300 °C, so, a long lifetime is expected when they would be used as catalysts for CO oxidation. Additionally, since a higher percentage of CO conversion was achieved for BM-A composition than for BM, it is confirmed that the partial substitution of Ba cation by Ce, La, or Mg is effective to improve the catalytic performance of raw BM samples. BM-La is the most effective catalyst as it is the most reducible and because it evolves α'-O_2.

Author Contributions: The individual contributions of each author are indicated as follows: N.G.: investigation, resources, data curation, and writing—original draft preparation; Á.D.V.: investigation and resources, writing—review and editing; M.J.I.G.: conceptualization, methodology, writing—review and editing, visualization, supervision, project administration, and funding acquisition. All authors have read and agreed to the published version of the manuscript.

Funding: This research was funded by the Spanish Government (MINCINN: PID2019-105542RB-I00/AEI/10.13039/501100011033 Project), the European Union (FEDER Funds), and Generalitat Valenciana (CIPROM/2021-070 Project). N. Ghezali thanks Argelian Government for her thesis grant and Á. Díaz-Verde of the University of Alicante for his predoctoral contract.

Data Availability Statement: Data are contained within the article.

Conflicts of Interest: The authors declare no conflicts of interest.

References

1. Dey, S.; Mehta, N.S. Automobile Pollution Control Using Catalysis. *Resour. Environ. Sustain.* **2020**, *2*, 100006. [CrossRef]
2. Bhandwal, M.; Tyagi, R.K. A New Method to Reduce the Harmful Gases and Particulate Matter Emitted from the Vehicles. *Mater. Today Proc.* **2022**, *56*, 3623–3626. [CrossRef]
3. Nadanakumar, V.; Jenoris Muthiya, S.; Prudhvi, T.; Induja, S.; Sathyamurthy, R.; Dharmaraj, V. Experimental Investigation to Control HC, CO & NO_x Emissions from Diesel Engines Using Diesel Oxidation Catalyst. *Mater. Today Proc.* **2021**, *43*, 434–440. [CrossRef]
4. Horizon Europe Work Programme for 2023–2024. Available online: https://cinea.ec.europa.eu/news-events/news/horizon-europe-work-programme-2023-24-now-available-2022-12-07_en (accessed on 9 October 2023).
5. Prasad, R.; Singh, P. A review on CO oxidation over copper chromite catalysts. *Catal. Rev.* **2012**, *54*, 224–279. [CrossRef]
6. Zhou, Y.; Wang, Z.; Liu, C. Perspective on CO oxidation over Pd-based catalysts. *Catal. Sci. Technol.* **2015**, *5*, 69–81. [CrossRef]
7. Grabchenko, M.B.; Mamontov, G.V.; Zaikovskii, V.I.; La Parola, V.; Liotta, L.F.; Vodyankina, O.V. The role of metal-support interaction in Ag/CeO_2 catalysts for CO and soot oxidation. *Appl. Catal. B. Environ.* **2020**, *260*, 118148. [CrossRef]
8. Zhang, N.; Li, L.; Wu, R.; Song, L.; Zheng, L.; Zhang, G.; He, H. Activity enhancement of Pt/MnO_x catalyst by novel β-MnO_2 for low-temperature CO oxidation: Study of the CO-O_2 competitive adsorption and active oxygen species. *Catal. Sci. Technol.* **2019**, *9*, 347–354. [CrossRef]
9. Zhang, L.L.; Sun, M.J.; Liu, C.G. CO oxidation on the phosphotungstic acid supported Rh single-atom catalysts via Rh-assisted Mans-van Krevelen mechanism. *Mol. Catal.* **2019**, *462*, 37–45. [CrossRef]
10. Zhang, Y.; Wu, Y.; Wang, H.; Guo, Y.; Wang, L.; Zhan, W.; Guo, Y.; Lu, G. The effects of the presence of metal Fe in the CO oxidation over Ir/FeO_x catalyst. *Catal. Commun.* **2015**, *61*, 83–87. [CrossRef]
11. Song, K.S.; Kang, S.K.; Kim, S.D. Preparation and Characterization of Ag/MnO_x/Perovskite Catalysts for CO Oxidation. *Catal. Lett.* **1997**, *49*, 65–68. [CrossRef]
12. Seyfi, B.; Baghalha, M.; Kazemian, H. Modified $LaCoO_3$ Nano-Perovskite Catalysts for the Environmental Application of Automotive CO Oxidation. *Chem. Eng. J.* **2009**, *148*, 306–311. [CrossRef]
13. Cui, X.; Liu, J.; Yan, X.; Yang, Y.; Xiong, B. Exploring Reaction Mechanism of CO Oxidation over $SrCoO_3$ Catalyst: A DFT Study. *Appl. Surf. Sci.* **2021**, *570*, 151234. [CrossRef]
14. Díaz-Verde, A.; Torregrosa-Rivero, V.; Illán-Gómez, M.J. Copper Catalysts Supported on Barium Deficient Perovskites for CO Oxidation Reaction. *Top. Catal.* **2023**, *66*, 895–907. [CrossRef]
15. Nie, L.; Mei, D.; Wang, Y. Activation of surface lattice oxygen in single-atom Pt/CeO_2 for low-temperature CO oxidation. *Science* **2017**, *358*, 1419–1423. [CrossRef]
16. Aneggi, E.; Trovarelli, A. Potential of ceria-zirconia-based materials in carbon soot oxidation for gasoline particulate filters. *Catalysts* **2020**, *10*, 768. [CrossRef]
17. Montini, T.; Melchionna, M.; Monai, M.; Fornasiero, P. Fundamentals and catalytic applications of CeO_2-based materials. *Chem. Rev.* **2016**, *116*, 5987–6041. [CrossRef]
18. Hernández, W.Y.; Tsampas, M.N.; Zhao, C.; Boreave, A.; Bosselet, F.; Vernoux, P. La/Sr-Based Perovskites as Soot Oxidation Catalysts for Gasoline Particulate Filters. *Catal. Today* **2015**, *258*, 525–534. [CrossRef]
19. Moreno-Marcos, C.; Torregrosa-Rivero, V.; Albaladejo-Fuentes, V.; Sánchez-Adsuar, M.S.; Illán-Gómez, M.J. $BaFe_{1-x}Cu_xO_3$ Perovskites as Soot Oxidation Catalysts for Gasoline Particulate Filters (GPF): A Preliminary Study. *Top. Catal.* **2019**, *62*, 413–418. [CrossRef]
20. Peron, G.; Glisenti, A. Perovskites as Alternatives to Noble Metals in Automotive Exhaust Abatement: Activation of Oxygen on $LaCrO_3$ and $LaMnO_3$. *Top. Catal.* **2019**, *62*, 244–251. [CrossRef]
21. Doggali, P.; Kusaba, S.; Teraoka, Y.; Chankapure, P.; Rayalu, S.; Labhsetwar, N. $La_{0.9}Ba_{0.1}CoO_3$ Perovskite Type Catalysts for the Control of CO and PM Emissions. *Catal. Commun.* **2010**, *11*, 665–669. [CrossRef]
22. Díaz-Verde, Á.; Montilla-Verdú, S.; Torregrosa-Rivero, V.; Illán-Gómez, M.J. Tailoring the Composition of Ba_xBO_3 (B = Fe, Mn) Mixed Oxides as CO or Soot Oxidation Catalysts in Simulated GDI Engine Exhaust Conditions. *Molecules* **2023**, *28*, 3327. [CrossRef]
23. Mokoena, L.; Pattrick, G.; Scurrell, M.S. Catalytic Activity of Gold-Perovskite Catalysts in the Oxidation of Carbon Monoxide. *Gold Bull.* **2016**, *49*, 35–44. [CrossRef]
24. Xiao, P.; Zhong, L.; Zhu, J.; Hong, J.; Li, J.; Li, H.; Zhu, Y. CO and Soot Oxidation over Macroporous Perovskite $LaFeO_3$. *Catal. Today* **2015**, *258*, 660–667. [CrossRef]

25. Assirey, E.A.R. Perovskite Synthesis, Properties and Their Related Biochemical and Industrial Application. *Saudi Pharm. J.* **2019**, *27*, 817–829. [CrossRef] [PubMed]
26. Zhang, L.; Filot, I.A.W.; Su, Y.-Q.; Liu, J.-X.; Hensen, E.J.M. Understanding the Impact of Defects on Catalytic CO Oxidation of $LaFeO_3$-Supported Rh, Pd, and Pt Single-Atom Catalysts. *J. Phys. Chem. C* **2019**, *123*, 7290–7298. [CrossRef] [PubMed]
27. Torregrosa-Rivero, V.; Sánchez-Adsuar, M.S.; Illán-Gómez, M.J. Improving the Performance of $BaMnO_3$ Perovskite as Soot Oxidation Catalyst Using Carbon Black during Sol-Gel Synthesis. *Nanomaterials* **2022**, *12*, 219. [CrossRef] [PubMed]
28. Feng, N.; Chen, C.; Meng, J.; Wu, Y.; Liu, G.; Wang, L.; Wan, H.; Guan, G. Facile Synthesis of Three-Dimensionally Ordered Macroporous Silicon-Doped $La_{0.8}K_{0.2}CoO_3$ Perovskite Catalysts for Soot Combustion. *Catal. Sci. Technol.* **2016**, *6*, 7718–7728. [CrossRef]
29. Torregrosa-Rivero, V.; Sánchez-Adsuar, M.S.; Illán-Gómez, M.J. Exploring the Effect of Using Carbon Black in the Sol-Gel Synthesis of $BaMnO_3$ and $BaMn_{0.7}Cu_{0.3}O_3$ Perovskite Catalysts for CO Oxidation. *Catal. Today* **2023**, *423*, 114028. [CrossRef]
30. Kembo, J.P.N.; Wang, J.; Luo, N.; Gao, F.; Yi, H.; Zhao, S.; Zhou, Y.; Tang, X. A Review of Catalytic Oxidation of Carbon Monoxide over Different Catalysts Emphasis on Hopcalite Catalysts. *New J. Chem.* **2023**, *44*, 20207. [CrossRef]
31. Atkins, P. *Shriver and Atkins' Inorganic Chemistry*; OUP: Oxford, UK, 2010; ISBN 978-0-19-923617-6.
32. Ghezali, N.; Díaz Verde, Á.; Illán Gómez, M.J. Screening $Ba_{0.9}A_{0\cdot1}MnO_3$ and $Ba_{0.9}A_{0.1}Mn_{0.7}Cu_{0.3}O_3$ (A = Mg, Ca, Sr, Ce, La) Sol-Gel Synthesised Perovskites as GPF Catalysts. *Materials* **2023**, *16*, 6899. [CrossRef] [PubMed]
33. Çoban Özkan, D.; Türk, A.; Celik, E. Synthesis and Characterizations of $LaMnO_3$ Perovskite Powders Using Sol–Gel Method. *J. Mater. Sci. Mater. Electron.* **2021**, *32*, 15544–15562. [CrossRef]
34. Díaz Verde, Á.; Martínez Munuera, J.C.; García García, A.; Piqueras, P.; Sanchis, E.G. Ceria and Praseodymia-Based Catalysts for the Removal of Gaseous Pollutants from Oxyfuel Combustion Engines. In Proceedings of the 15th European Congress on Catalysis, Prague, Czech Republic, 27 August–1 September 2023.
35. Aarif Ul Islam, S.; Ikram, M. Structural Stability Improvement, Williamson Hall Analysis and Band-Gap Tailoring through A-Site Sr Doping in Rare Earth Based Double Perovskite La_2NiMnO_6. *Rare Met.* **2019**, *38*, 805–813. [CrossRef]
36. Akinlolu, K.; Omolara, B.; Shailendra, T.; Abimbola, A.; Kehinde, O. Synthesis, Characterization and Catalytic Activity of Partially Substituted $La_{1-x}Ba_xCoO_3$ ($x \geq 0.1 \leq 0.4$) Nano Catalysts for Potential Soot Oxidation in Diesel Particulate Filters in Diesel Engines. *Int. Rev. Appl. Sci. Eng.* **2020**, *11*, 52–57. [CrossRef]
37. Torregrosa-Rivero, V.; Sánchez-Adsuar, M.-S.; Illán-Gómez, M.-J. Modified $BaMnO_3$-Based Catalysts for Gasoline Particle Filters (GPF): A Preliminary Study. *Catalysts* **2022**, *12*, 1325. [CrossRef]
38. Torregrosa-Rivero, V.; Albaladejo-Fuentes, V.; Sánchez-Adsuar, M.-S.; Illán-Gómez, M.-J. Copper Doped $BaMnO_3$ Perovskite Catalysts for NO Oxidation and NO_2-Assisted Diesel Soot Removal. *RSC Adv.* **2017**, *7*, 35228–35238. [CrossRef]
39. Albaladejo-Fuentes, V.; Sánchez-Adsuar, M.S.; Illán-Gómez, M.-J. Tolerance and Regeneration versus SO_2 of $Ba_{0.9A0.1}Ti_{0.8}Cu_{0.2}O_3$ (A = Sr, Ca, Mg) Catalysts. *Appl. Catal. A Gen.* **2019**, *577*, 113–123.
40. Koolen, C.D.; Luo, W.; Züttel, A. From Single Crystal to Single Atom Catalysts: Structural Factors Influencing the Performance of Metal Catalysts for CO_2 Electroreduction. *ACS Catal.* **2023**, *13*, 948–973. [CrossRef]
41. Wang, H.; Liu, J.; Zhao, Z.; Wei, Y.; Xu, C. Comparative Study of Nanometric Co-, Mn- and Fe-Based Perovskite-Type Complex Oxide Catalysts for the Simultaneous Elimination of Soot and NOx from Diesel Engine Exhaust. *Catal. Today* **2012**, *184*, 288–300. [CrossRef]
42. Zhao, Z.; Yamada, Y.; Ueda, A.; Sakurai, H.; Kobayashi, T. The Roles of Redox and Acid–Base Properties of Silica-Supported Vanadia Catalysts in the Selective Oxidation of Ethane. *Catal. Today* **2004**, *93–95*, 163–171. [CrossRef]
43. Liu, X.; Wang, Y.; Zang, M.; Shi, L.; Zhang, H.; Zhao, C. Effect of A-Site Element on the Performance of Three-Dimensionally Ordered Macroporous Manganese-Based Perovskite Catalyst. *J. Saudi Chem. Soc.* **2020**, *24*, 417–424. [CrossRef]
44. Zang, M.; Zhao, C.; Wang, Y.; Liu, X.; Cheng, Y.; Chen, S. Low Temperature Catalytic Combustion of Toluene over Three-Dimensionally Ordered $La_{0.8}Ce_{0.2}MnO_3$/Cordierite Catalysts. *Appl. Surf. Sci.* **2019**, *483*, 355–362. [CrossRef]
45. Yi, Y.; Liu, H.; Chu, B.; Qin, Z.; Dong, L.; He, H.; Tang, C.; Fan, M.; Bin, L. Catalytic Removal NO by CO over $LaNi_{0.5}M_{0.5}O_3$ (M = Co, Mn, Cu) Perovskite Oxide Catalysts: Tune Surface Chemical Composition to Improve N2 Selectivity. *Chem. Eng. J.* **2019**, *369*, 511–521. [CrossRef]
46. Kapteijn, F.; Singoredjo, L.; Andreini, A.; Moulijn, J.A. Activity and Selectivity of Pure Manganese Oxides in the Selective Catalytic Reduction of Nitric Oxide with Ammonia. *Appl. Catal. B Environ.* **1994**, *3*, 173–189. [CrossRef]
47. Khaskheli, A.A.; Xu, L.; Liu, D. Manganese Oxide-Based Catalysts for Soot Oxidation: A Review on the Recent Advances and Future Directions. *Energy Fuels* **2022**, *36*, 7362–7381. [CrossRef]
48. Zhang, C.; Wang, C.; Hua, W.; Guo, Y.; Lu, G.; Gil, S.; Giroir-Fendler, A. Relationship between Catalytic Deactivation and Physicochemical Properties of $LaMnO_3$ Perovskite Catalyst during Catalytic Oxidation of Vinyl Chloride. *Appl. Catal. B Environ.* **2016**, *186*, 173–183. [CrossRef]
49. Wang, Y.; Arandiyan, H.; Scott, J.; Akia, M.; Dai, H.; Deng, J.; Aguey-Zinsou, K.-F.; Amal, R. High Performance Au–Pd Supported on 3D Hybrid Strontium-Substituted Lanthanum Manganite Perovskite Catalyst for Methane Combustion. *ACS Catal.* **2016**, *6*, 6935–6947. [CrossRef]
50. Cimino, S.; Colonna, S.; De Rossi, S.; Faticanti, M.; Lisi, L.; Pettiti, I.; Porta, P. Methane Combustion and CO Oxidation on Zirconia-Supported La, Mn Oxides and $LaMnO_3$ Perovskite. *J. Catal.* **2002**, *205*, 309–317. [CrossRef]

51. Peña, M.A.; Fierro, J.L.G. Chemical Structures and Performance of Perovskite Oxides. *Chem. Rev.* **2001**, *101*, 1981–2018. [CrossRef] [PubMed]
52. Li, Z.; Wang, X.; Li, X.; Zeng, M.; Redshaw, C.; Cao, R.; Sarangi, R.; Hou, C.; Chen, Z.; Zhang, W.; et al. Engineering Surface Segregation of Perovskite Oxide through Wet Exsolution for CO Catalytic Oxidation. *J. Hazard. Mater.* **2022**, *436*, 129110. [CrossRef] [PubMed]
53. Zheng, S.; Hua, Q.; Gu, W.; Liu, B. Catalytic Oxidation of CO on $LaMn_{1-x}Fe_xO_3$ Perovskites Solid Solution. *J. Mol. Catal. A Chem.* **2014**, *391*, 7–11. [CrossRef]
54. Gremminger, A.; Pihl, J.; Casapu, M.; Grunwaldt, J.-D.; Toops, T.J.; Deutschmann, O. PGM Based Catalysts for Exhaust-Gas after-Treatment under Typical Diesel, Gasoline and Gas Engine Conditions with Focus on Methane and Formaldehyde Oxidation. *Appl. Catal. B Environ.* **2020**, *265*, 118571. [CrossRef]
55. Yang, Q.; Li, J.; Wang, D.; Peng, Y.; Ma, Y. Activity Improvement of Acid Treatment on LaFeO3 Catalyst for CO Oxidation. *Catal. Today* **2021**, *376*, 205–210. [CrossRef]
56. York, A.P.E.; Cooper, C.S.; Simmance, K.; Wilkinson, S.K. Non-PGM Iron Perovskite Three-Way Gasoline Emissions Control Catalysts: Kinetics, Reaction Mechanism and Catalyst Sizing Study. *Top. Catal.* **2020**, *63*, 256–267. [CrossRef]
57. Zhang-Steenwinkel, Y.; van der Zande, L.M.; Castricum, H.L.; Bliek, A. Step Response and Transient Isotopic Labelling Studies into the Mechanism of CO Oxidation over $La_{0.8}Ce_{0.2}MnO_3$ Perovskite. *Appl. Catal. B Environ.* **2004**, *54*, 93–103. [CrossRef]
58. Yang, J.; Hu, S.; Fang, Y.; Hoang, S.; Li, L.; Yang, W.; Liang, Z.; Wu, J.; Hu, J.; Xiao, W.; et al. Oxygen Vacancy Promoted O2 Activation over Perovskite Oxide for Low-Temperature CO Oxidation. *ACS Catal.* **2019**, *9*, 9751–9763. [CrossRef]
59. Loc, L.C.; Tri, N.; Cuong, H.; Gaidai, N.; Agafonov, Y.; Nekrasov, N.V.; Ha, A.; Thoang, H.S.; Lapidus, A.L. Mechanism of Carbon Monoxide Oxidation over Supported CuO Catalysts Modified by Ce and Pt. *DGMK Tagungsbericht* **2014**, *2014*, 167–176.
60. Royer, S.; Duprez, D. Catalytic Oxidation of Carbon Monoxide over Transition Metal Oxides. *ChemCatChem* **2011**, *3*, 24–65. [CrossRef]
61. Ding, K.; Gulec, A.; Johnson, A.M.; Schweitzer, N.M.; Stucky, G.D.; Marks, L.D.; Stair, P.C. Identification of Active Sites in CO Oxidation and Water-Gas Shift over Supported Pt Catalysts. *Science* **2015**, *350*, 189–192. [CrossRef]
62. Schmal, M.; Perez, C.A.C.; Magalhães, R.N.S.H. Synthesis and Characterization of Perovskite-Type Oxides $La_{1-x}M_xCoO_3$ (M = Ce, Sr) for the Selective CO Oxidation (SELOX). *Top. Catal.* **2014**, *57*, 1103–1111. [CrossRef]